The combined effect of size, inertia and porosity on the indentation response of ductile materials

T. dos Santos[a], A. Srivastava[b], J. A. Rodríguez-Martínez[c,*]

[a] *Departamento de Engenharia Mecânica, Universidade Federal de Santa Maria, Av. Roraima, 1000, Prédio 7, Santa Maria, RS, 97105-900, Brazil.*

[b] *Department of Materials Science and Engineering, Texas A&M University, College Station, TX, USA*

[c] *Department of Continuum Mechanics and Structural Analysis, University Carlos III of Madrid, Avda. de la Universidad, 30, 28911 Leganés, Madrid, Spain*

Abstract

Herein, we present a self-similar cavity expansion model that follows from the work of Cohen and Durban (2013b) to analyze the dynamic indentation response of elasto-plastic porous materials while accounting for the plastic strain gradient induced size effect. The incorporation of the plastic strain gradient induced size effect in the dynamic cavity expansion model for elasto-plastic porous materials is the key novelty of our model. The predictions of the cavity expansion model for the material hardness, for different indentation depths and speeds, are compared against the available experimental results for OFHC copper, for strain rates varying from 10^{-4} s^{-1} to 10^{8} s^{-1}. We note that despite several simplifying assumptions, the predictions of our cavity expansion model show a reasonable agreement with the experimentally measured material hardness over a wide range of indentation depths and speeds. In addition, we have also carried out parametric analyses to elucidate the specific roles of indentation speed, size effect and initial porosity, on the material hardness and cavitation fields that develop during the indentation process. In particular, our parametric analyses show that there exists a critical value of the indentation speed beyond which the contribution of inertial effect becomes extremely important and the material hardness increases rapidly. While the influence of the initial porosity on the material hardness is found to increase with increasing indentation speed and decrease with increasing size effect.

Keywords:

Dynamic indentation, Cavity expansion, size effect, Ductile materials, Porous plasticity

---

1. Introduction

Mok and Duffy (1964) published one of the first experimental works on impact indentation of metallic materials. They dropped balls of hardened steel and aluminum of 12.7 mm and 25.4 mm diameter onto targets of pure lead and AA6061-T6, at a range of velocities (with a maximum of 6 m/s) giving strain rates varying

*Corresponding author. Tel. +34 916249904; Fax: +33 916249430. E-mail address:jarmarti@ing.uc3m.es

from quasi-static to $\approx 3 \cdot 10^3$ s^{-1}, and temperatures ranging from 295 K to 750 K. In these experiments, they measured the impact and rebound velocities, as well as the size of the crater formed in the target and the time of contact between the impactor and the target. Next, using a simple energy balance, equating the loss in kinetic energy of the impactor to the energy required to produce the indentation, Mok and Duffy (1964) determined the dynamic yield pressure (i.e. hardness) of the target for each test. At room temperature, in the case of pure lead, the dynamic yield pressure varied from 20 MPa for quasi-static loading to 70 MPa for the highest strain rate tested, and from 200 to 400 MPa in the case of AA6061-T6. These experiments provided the first evidence that material hardness changes with the impact velocity. Shortly after, Mok and Duffy (1965) performed additional tests on C1018 steel and AA 1100F. These experiments were performed at room temperature and for the same range of impact velocities as in Mok and Duffy (1964). These additional tests confirmed the dependence of the material hardness on the strain rate, and showed that results of dynamic indentation experiments can be interpreted to provide a measure of the yield stress of the target material over a range of strain rates.

Later, Tirupataiah and Sundararajan (1991) published what is probably the first experimental work on very high velocity impact indentation of metallic materials. These authors launched very hard spherical tungsten carbide balls of 4.75 mm diameter onto iron and copper targets at velocities ranging from 5 m/s to 180 m/s. Similar to Mok and Duffy (1964, 1965), the dynamic hardness of the material was defined as the resistance per unit area opposing the penetration of the ball, and it was calculated from an energy balance between the kinetic energy of the projectile and the energy required to form the resulting crater in the target, under the assumption that all the energy of the impacting ball (except for the rebound energy) was consumed in the plastic deformation of the target material. The experiments showed that material hardness generally increases under dynamic loading, reaching 800 MPa for copper and 1600 MPa for iron, and becoming up to three times higher than under quasi-static conditions for strain rates that were estimated to be as high as $\approx 10^4$ s^{-1}. Tirupataiah and Sundararajan (1991) also brought out some limitations of the high velocity dynamic indentation tests, including the fact that the proper determination of the dynamic hardness requires the material to harden during the indentation process. Sundararajan and Tirupataiah (2006) performed additional experiments with copper, iron, steel, and AA7039 alloy samples, and showed that for the last three materials the dynamic hardness measured in the experiments displays a maximum for a critical strain, and then decreases due to the onset of plastic localization, which was attributed to the decrease in flow stress due to the adiabatic heating of the material.

Thirty-five years after the pioneering works of Mok and Duffy (1964, 1965), Subhash et al. (1999) developed an experimental setup to perform dynamic indentation tests, using the one-dimensional elastic wave propagation principle employed in Kolsky bar experiments, which allowed them to obtain time-resolved indentation depth and load responses during the indentation process. Subhash et al. (1999) tested a variety of materials and the maximum strain rate attained in these experiments was $\approx 2 \cdot 10^3$ s^{-1}. Their experimental results showed that, for this high strain rate, the increase in dynamic hardness over quasi-static hardness depends on the material, ranging from 2% for aluminum to 30% for titanium. Later, Lu et al. (2003) developed an alternative dynamic indentation technique which enabled recording of the force and displacement of the indenter for test velocities ranging from 6 m/s to 35 m/s. In these experiments, the measured indentation depth and load were used to estimate the strain rate sensitivity of OFHC copper, and the results obtained were shown to be in agreement with the data obtained with Kolsky bar experiments. More recently, Hassani et al. (2020) have developed an experimental setup to perform microparticle impact indentation to determine material hardness at strain rates beyond 10^6 s^{-1} (these are probably the first measurements of hardness at such high strain rates). These authors employed laser ablation to impact ceramic alumina microparticles of 14 μm diameter (as indenter) onto copper and iron targets, and obtained time-resolved measurements of the impact and rebound velocities together with post-impact measurements of the volume of the indent. Similarly to Tirupataiah and Sundararajan (1991), Hassani et al. (2020) calculated the dynamic hardness of the target material as the ratio of the plastic work to the indentation volume, and showed that, for strain rates greater than 10^6 s^{-1}, the hardness of the material increases up to $4 - 5$ GPa, i.e. it becomes one order of magnitude greater than under quasi-static loading conditions.

Besides dynamic effect, size effect has also been shown to play an important role on the indentation response of a variety of materials, and it is generally observed that the hardness of the material increases as the size of the indent decreases. For instance, Poole et al. (1996) performed quasi-static micro-indentation experiments on annealed and work hardened copper specimens and showed a monotonic increase in the hardness for indentation depths below ≈ 10 μm. The experimental results were explained using a dislocation-based model which incorporated geometrically necessary dislocations due to the presence of strain gradients in the deformation zone around the indent. Later, McElhaney et al. (1998) obtained accurate measurements of the hardness of copper for indentation depths near 100 nm. For such a small indentation depth, the material hardness was found to be above 2 GPa, i.e. $4 - 5$ times higher than the value corresponding to the greater indentation depth (≈ 2000 nm) tested. Moreover, the quasi-static nano-indentation experiments on copper performed by Lim and Chaudhri (1999) yielded the same trends obtained in the tests of Poole et al. (1996) and McElhaney et al. (1998), with greater hardness for small indentation depth.

A number of experimental studies have also focused on the combined effect of inertia and various size effects on the material hardness. Trelewicz and Schuh (2008) were among the first authors to perform high strain rate nano-indentation experiments. These authors tested nanocrystalline Ni-W samples with grain sizes ranging from 3 to 150 nm. In these tests, the maximum penetration depth was 1 μm and the characteristic strain rate was estimated to be $\approx 10^3$ s^{-1}. Trelewicz and Schuh (2008) found $\approx 10\%$ increase in the material hardness under dynamic loading as compared to the quasi-static loading for grain sizes below 40 nm. Using similar setup to Trelewicz and Schuh (2008), Arreguin-Zavala et al. (2013) performed nano-impact indentation experiments on nanostructured and ultrafine-grained Al-Si claddings at various temperatures ranging from 623 K to 773 K. The dynamic hardness was found to increase nonlinearly as the penetration depth decreases, from ≈ 1.5 GPa for 6 μm to ≈ 3.5 GPa for 2.5 μm. Later, Qin et al. (2019) determined the dynamic hardness of single crystal Al (110) at strain rates that were estimated to be $\approx 10^4$ s^{-1} at the first stages of the indentation process. The comparison of the high strain rate experimental results with quasi-static nano-indentation tests showed that the dynamic hardness of Al (110) single crystals is not only greater but is also more sensitive to size effect.

Mathematical modeling of the indentation process of metallic materials is in general based on the cavity expansion model following the pioneering work of Johnson (1970), who considered that the indenter is encased in a semi-cylindrical or hemispherical core (the cavity) subjected to hydrostatic pressure equal to the indentation pressure, and the core expands (i.e. material displaces radially) as the indenter penetrates the specimen. While outside the core, the stress and strain fields are considered to be radially symmetric and are the same as in an infinite body containing a cylindrical or spherical cavity under pressure. Johnson (1970) obtained quasi-static solutions for elastic perfectly-plastic materials, and validated the theoretical results with experimental data obtained with different wedge-shape indenters. Later, Fleck et al. (1992) extended the cavity expansion model of Johnson (1970) to elasto-plastic porous solids. These authors compared the theoretical results with finite element calculations, and showed that for nearly rate-independent porous materials, the cavity expansion model provides accurate qualitative predictions of the effect of porosity, elastic modulus and indenter angle on the quasi-static indentation pressure. Mata et al. (2006) and Gao et al. (2006) revisited the analogy between indentation experiments and cavity expansion, and developed a quasi-static cavity expansion model for strain hardening elasto-plastic solids. These works led to closed-form solutions for the extension of the plastic zone that develops near the indenter (Mata et al., 2006) and demonstrated that for a given indenter geometry, indentation hardness depends on Young's modulus, yield stress and strain-hardening exponent of the material (Gao et al., 2006). The plastic strain gradient induced size effect is also incorporated in the quasi-static cavity expansion model by Gao (2006). In line with the experimental observations, Gao (2006) obtained the indentation size dependent hardness of the material under quasi-static loading conditions (smaller the indentation depth, greater the hardness of the material).

Note that all the works discussed in the preceding paragraph are for the quasi-static indentation problems. This is despite the fact that numerous experimental works (as detailed in the earlier paragraphs) have highlighted the effects of dynamics and indentation size at high loading rates. Thus, here we present a dynamic cavity expansion model to analyze the high rate indentation response of elasto-plastic porous materials while accounting for the plastic strain gradient induced size effect. We note that dynamic cavity expansion models have been utilized to study the mechanisms of deep penetration and perforation in structural impact problems (e.g. Cohen and Durban (2013a)). However, their extension and application to estimate dynamic hardness of the material in which the inertial forces and size effects are important has not been addressed before (to the best of our knowledge). The remainder of the paper is organized as follows. Section 2 describes the elasto-plastic constitutive framework used to model the material behaviour, in which yielding is described using the modified Gurson flow potential while incorporating the size effect following the work of Chen and Yuan (2002). The dynamic spherical cavity expansion model used to analyze dynamic indentation is developed in Section 3. Section 4 compares the results of the theoretical model with experimental results of Poole et al. (1996), McElhaney et al. (1998), Lim and Chaudhri (1999) and Hassani et al. (2020) for annealed OFHC copper, showing that the cavity expansion model developed herein very well captures the increase in material hardness with decreasing indentation depth and increasing strain rate. The results of parametric analyses elucidating the specific roles of indentation speed, size effect and initial porosity, on the material hardness and cavitation fields that develop during the indentation process are also presented in Section 4. Finally, the main conclusions derived from this work are listed in Section 5.

2. Constitutive framework

This section describes the elasto-plastic constitutive framework used to model the mechanical behavior of the porous material. Here, yielding is described by the *heuristic* modification of the Gurson-Tvergaard flow potential as proposed by Chen and Yuan (2002) in which the size effect is included through by definition of the flow strength of the matrix material.

The rate of the deformation tensor, $\boldsymbol{d}$, is taken to be the sum of an elastic part, $\boldsymbol{d}^e$, and a plastic part, $\boldsymbol{d}^p$:

$$\boldsymbol{d} = \boldsymbol{d}^e + \boldsymbol{d}^p \tag{1}$$

with the elastic part being related to the rate of the Cauchy stress tensor $\boldsymbol{\sigma}$ by the following hypo-elastic law:

$$\overset{\triangledown}{\boldsymbol{\sigma}} = \boldsymbol{C} : \boldsymbol{d}^e \tag{2}$$

where $\overset{\triangledown}{()}$ denotes an objective derivative and $\boldsymbol{C}$ is the fourth order isotropic elastic tensor given as:

$$\boldsymbol{C} = \frac{E}{1+\nu}\boldsymbol{I}' + \frac{E}{3\,(1-2\nu)}\mathbf{1}\otimes\mathbf{1} \tag{3}$$

where E is the Young's modulus, ν the Poisson's ratio, $\mathbf{1}$ the unit second order tensor and $\boldsymbol{I}'$ the unit-deviatoric fourth order tensor.

The plastic part of the rate of deformation tensor is written as:

$$\boldsymbol{d}^p = \dot{\lambda}\frac{\partial \Phi}{\partial \boldsymbol{\sigma}} \tag{4}$$

where $\dot{\lambda}$ is the rate of plastic multiplier and Φ is the plastic flow potential:

$$\Phi = \left(\frac{\sigma_e}{\bar{\sigma}}\right)^2 + 2q_1 f \cosh\left(\frac{3q_2\sigma_h}{2\bar{\sigma}}\right) - 1 - (q_1 f)^2 \leq 0 \tag{5}$$

where q_1 and q_2 are material parameters and f is the void volume fraction (see equation (9)). The effective von Mises effective stress, σ_e, and the hydrostatic stress, σ_h, are:

$$\sigma_e = \sqrt{\frac{3}{2}\boldsymbol{s} : \boldsymbol{s}}, \quad \sigma_h = \frac{1}{3}\boldsymbol{\sigma} : \mathbf{1}, \quad \boldsymbol{s} = \boldsymbol{\sigma} - \sigma_h \mathbf{1}$$

with $\boldsymbol{s}$ being the deviatoric part of the Cauchy stress tensor. Similarly to Chen and Yuan (2002), the flow strength of the matrix material $\bar{\sigma}$ is defined using a simple form of the generalized gradient plasticity model proposed by Aifantis (1984):

$$\bar{\sigma} = \bar{\sigma}_{hom}\left(\bar{\varepsilon}^p, T\right) + E\, l\, \|\nabla\bar{\varepsilon}^p\| \tag{6}$$

where E is the Young's modulus (as mentioned before), l is the length scale parameter and $\|\nabla\bar{\varepsilon}^p\| = \left(\nabla\bar{\varepsilon}^p \cdot \nabla\bar{\varepsilon}^p\right)^{\frac{1}{2}}$ stands for the Euclidean norm of $\nabla\bar{\varepsilon}^p$, with $\bar{\varepsilon}^p = \int_0^t \dot{\bar{\varepsilon}}^p(\tau)\, d\tau$ being the effective plastic strain in the matrix material and $\dot{\bar{\varepsilon}}^p$ the effective plastic strain rate. The advantages of this simple gradient plasticity model are that it introduces a single length scale parameter and dismisses high order derivatives, which greatly facilitates the formulation of the dynamic cavity expansion model and the interpretation of results. Note that, for the sake of simplicity, we have considered that the parameter l is constant. Here $\bar{\sigma}_{hom}$ is the flow strength for homogeneous deformation that depends on the effective plastic strain in the matrix material $\bar{\varepsilon}^p$ and the temperature T as follows:

$$\bar{\sigma}_{hom}\left(\bar{\varepsilon}^p, T\right) = \sigma_0\left(1 + \frac{\bar{\varepsilon}^p}{\varepsilon_0}\right)^n \left(1 + b\exp^{-c\,(T_0-273)}\left(\exp^{-c(T-T_0)} - 1\right)\right) \tag{7}$$

where σ_0 is the initial yield stress of the matrix material, n is the strain hardening exponent, ε_0 is the reference strain, and b, c and T_0 are parameters that determine the temperature sensitivity of the material.

The equality between the rates of macroscopic plastic work and matrix plastic work (Chen and Yuan, 2002):

$$\boldsymbol{\sigma} : \boldsymbol{d}^p = (1 - f)\,\bar{\sigma}\dot{\bar{\varepsilon}}^p \tag{8}$$

provides a relation between the plastic part of the rate of deformation tensor and the effective plastic strain rate in the matrix material.

Next, assuming the plastic incompressibility of the matrix material, the evolution of the void volume fraction is given as:

$$\dot{f} = (1 - f)\,\boldsymbol{d}^p : \mathbf{1} \tag{9}$$

Furthermore, assuming adiabatic conditions and considering that plastic work is the only source of heating, the temperature evolution is calculated as:

$$\rho C_p \dot{T} = \chi \boldsymbol{\sigma} : \boldsymbol{d}^p \tag{10}$$

with ρ, C_p and χ being the current material density, the specific heat and the Taylor-Quinney coefficient, respectively.

The values of the parameters of the constitutive model used in the cavity expansion calculations presented in Section 4 are given in Table 1. The flow strength for homogeneous deformation has been calibrated against the experimental results for annealed OFHC copper by Tanner and McDowell (1999). The elastic parameters, the initial material density and the specific heat also correspond to copper, and the standard values used in the literature are taken for the flow potential parameters q_1 and q_2, and the Taylor-Quinney factor χ. In the analysis performed in Section 4, parametric calculations are carried out for the values of the initial void volume fraction, f_0 and the length scale parameter, l.

Note that, for the sake of simplicity, we have not considered the strain rate dependence of the flow strength of the matrix material. While we are aware that this is a rather crude assumption for most metallic materials, it greatly facilitates the derivation of the theoretical model in Section 3 (rate-independent materials allow for self-similar cavity expansion solutions) and to interpret the results presented in Section 4 (isolating the effect of inertia in the cavitation fields at high strain rates). Note that including the strain rate sensitivity of the material in the constitutive model also introduces a time scale into the cavity expansion problem, see dos

Symbol	Property and units	Value
ρ_0	Initial density (kg/m^3)	8940
C_p	Specific heat (J/kg K), Eq. (10)	384.6
E	Young modulus (GPa), Eq. (3)	116
ν	Poisson ratio, Eq. (3)	0.31
q_1	Material parameter, Eq. (5)	1.25
q_2	Material parameter, Eq. (5)	1.0
f_0	Initial void volume fraction, Eq. (5)	0.0, 0.05, 0.1
σ_0	Reference yield stress (MPa), Eq. (7)	55
n	Strain hardening sensitivity parameter, Eq. (7)	0.32
l	Length scale parameter (nm), Eq. (6)	0, 10, 20, 30, 50
ε_0	Reference strain, Eq. (7)	0.0026
b	Temperature sensitivity parameter, Eq. (7)	10
c	Temperature sensitivity parameter (K^{-1}), Eq. (7)	1.23×10^{-4}
T_0	Reference temperature (K), Eq. (7)	293
χ	Taylor-Quinney coefficient, Eq. (10)	0.9

Table 1: Values of the parameters of the constitutive model used in the cavity expansion calculations presented in Section 4.

Santos et al. (2020).

The Gurson porous plasticity model was derived based on several assumptions, including that the shape of the void remains spherical during the whole loading process (i.e. high triaxiality loadings). However, the Gurson model has been in general employed to simulate the response of porous materials subjected to indentation and penetration and has been shown to provide results that are more or less consistent with the experimental observations. For instance, Cohen and Durban (2013a) derived a cavity expansion model to calculate the penetration resistance of highly porous titanium plates, and the analytical results were in reasonable accord with experimental data reported in the literature, showing a decrease in the ballistic limit with increase in material porosity. Nevertheless, a future work will be to extend the analytical model presented in this paper to also consider other damage mechanisms that develop in the material during indentation such as, nucleation of secondary voids and shear softening and localization due to pre-existing voids.

3. Dynamic indentation model

In this section, we extend the self-similar cavity expansion model developed by Cohen and Durban (2013b) for high velocity penetration problems to model dynamic indentation of rate-independent elasto-plastic porous solids exhibiting size effect. The mechanical behavior of the material is described using the constitutive framework presented in Section 2.

Following Johnson (1970), the process of conical indentation is idealized by the radial expansion of a spherical cavity. The main assumption is that the indenter is encased in a rigid hemispherical core of radius, a, (the expanding cavity) which is subjected to a hydrostatic stress equal to the indentation pressure, p, see Fig. 1. This approach considers that neither pile-up nor sink-in of the free surface of the material occurs during the indentation. While this is a rough assumption, the works of Johnson (1970) and Fleck et al. (1992), among others, have shown that it is a reasonable approximation for a variety of metallic materials.

Let us consider an Eulerian spherical coordinate system (r, θ, ϕ) with the origin located at the center of the hydrostatic core O, see Fig. 1. The indenter penetrates the solid at a constant velocity $\dot{h}$, such that a steady state indentation pressure is achieved whereby p does not change with time, thus causing the material to displace radially at velocity $\dot{r}$ (i.e. $\dot{r}$ is the radial velocity of a material point), see Fleck et al. (1992). The incompressibility of the material leads to the following relation (Johnson, 1970; Fleck et al., 1992):

$$2\dot{r} = \dot{h} \ \text{ at } \ r = a \quad \textit{(the cavity wall)} \tag{11}$$

where $\dot{h} = \dot{a} \tan\beta$ by geometry (see Fig. 1). Thus, the material velocity, $\dot{r}$, at $r = a$ relates to the core expansion velocity, $\dot{a}$, by:

$$\frac{\dot{r}}{\dot{a}} = \frac{\tan\beta}{2} \ \text{ at } \ r = a \quad \textit{(the cavity wall)} \tag{12}$$

Following Johnson (1970) and Fleck et al. (1992) and Danas et al. (2012), among others, in all the calculations presented in this work the cone angle β is taken as 19.7° in order to give the same displaced volume as the Vickers pyramid. Note that, for this cone angle, the material and the hydrostatic core (cavity) do not expand at the same speed, i.e. $\dot{r} \neq \dot{a}$. In fact, for $\beta < 63.43^{\circ}$, the velocity of the cavity is greater than the velocity of the material.

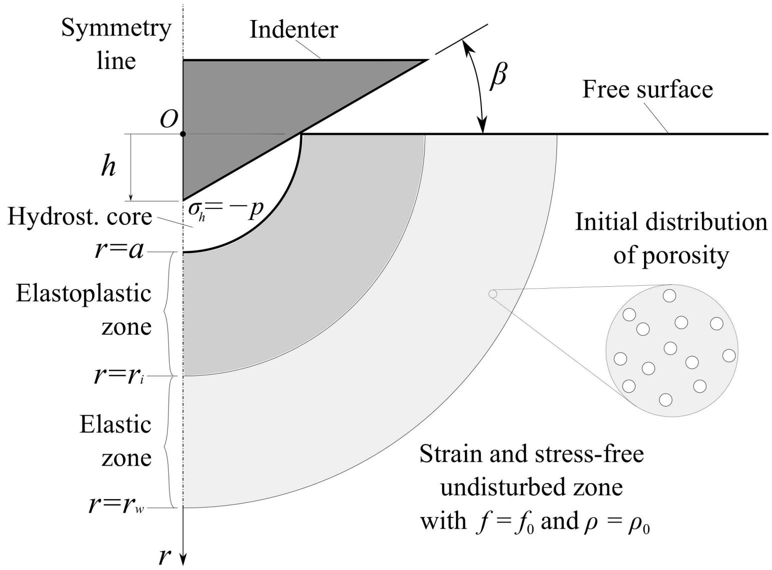

Figure 1: Illustration of the indentation problem.

Following Durban and Masri (2004), we take the non-dimensional radial coordinate $\xi = {}^{r}/_{a}$ as the only independent variable of the problem (self-similar steady-state solution). Accordingly, the derivative with respect to the radial coordinate is:

$$\frac{\partial\,()}{\partial r} = \frac{\partial\,()}{\partial \xi}\frac{\partial \xi}{\partial r} = ()'\,\frac{1}{a} \tag{13}$$

where the prime superscript denotes differentiation with respect to ξ. In addition, the time derivative is:

$$\dot{()} = \frac{\partial\,()}{\partial \xi}\dot{\xi} = ()'\,\frac{\dot{a}}{a}\,(v - \xi) \tag{14}$$

with $v = {}^{\dot{r}}/_{\dot{a}}$ being the dimensionless radial velocity. Since $\dot{a}$ is assumed to be constant (because $\dot{h}$ is assumed to be constant), the dimensionless acceleration is $\dot{v} = {}^{\ddot{r}}/_{\dot{a}}$.

Due to the spherical symmetry of the problem, the only active components of the Cauchy stress tensor are σ_{rr} and $\sigma_{\theta\theta} = \sigma_{\phi\phi}$. Hence, the linear momentum balance reduces to a single equation in the radial direction:

$$\frac{\partial \sigma_{rr}}{\partial r} + \frac{2}{r}\left(\sigma_{rr} - \sigma_{\theta\theta}\right) = \rho \ddot{r} \tag{15}$$

which, employing equations (13) and (14), is rewritten as:

$$\Sigma_{rr}' + \frac{2}{\xi}\left(\Sigma_{rr} - \Sigma_{\theta\theta}\right) = m^2 \frac{\rho}{\rho_0}\left(v - \xi\right) v' \tag{16}$$

where $\Sigma_{rr} = {}^{\sigma_{rr}}/_{E}$ and $\Sigma_{\theta\theta} = {}^{\sigma_{\theta\theta}}/_{E}$ are the dimensionless radial and circumferential stresses, respectively, and

$m = \dot{a}/\sqrt{E/\rho_0}$ is the ratio between $\dot{a}$ and the elastic wave velocity in a long rod $\sqrt{E/\rho_0}$, with ρ_0 being the initial material density.

Moreover, the only active components of the rate of deformation tensor are:

$$d_{rr} = \frac{\partial \dot{r}}{\partial r} \tag{17}$$

$$d_{\theta\theta} = d_{\phi\phi} = \frac{\dot{r}}{r} \tag{18}$$

The hypo-elastic law introduced in equation (2) can be rewritten as:

$$d^e_{rr} = \frac{1}{E}\dot{\sigma}_{rr} - \frac{2\nu}{E}\dot{\sigma}_{\theta\theta} \tag{19}$$

$$d^e_{\theta\theta} = d^e_{\phi\phi} = \frac{(1-\nu)}{E}\dot{\sigma}_{\theta\theta} - \frac{\nu}{E}\dot{\sigma}_{rr} \tag{20}$$

where in absence of material spin, the objective derivative $\overset{\triangledown}{()}$ (see equation (2)) has been replaced by a time derivative $\dot{()}$.

Furthermore, using the flow potential (5), and the plastic work equivalence (8), the flow rule given by equation (4) can be expressed as:

$$d^p_{rr} = (1-f)\,\dot{\bar{\varepsilon}}^p\,\tilde{N}_{rr} \tag{21}$$

$$d^p_{\theta\theta} = d^p_{\phi\phi} = (1-f)\,\dot{\bar{\varepsilon}}^p\,\tilde{N}_{\theta\theta} \tag{22}$$

with

$$\tilde{N}_{rr} = \frac{1}{2}\frac{-2\frac{\Sigma_e}{\bar{\Sigma}} + q_1 q_2 f \sinh\left(\frac{3q_2\Sigma_h}{2\bar{\Sigma}}\right)}{\left(\frac{\Sigma_e}{\bar{\Sigma}}\right)^2 + q_1 q_2 f \sinh\left(\frac{3q_2\Sigma_h}{2\bar{\Sigma}}\right)\frac{3\Sigma_h}{2\bar{\Sigma}}} \tag{23}$$

$$\tilde{N}_{\theta\theta} = \frac{1}{2}\frac{\frac{\Sigma_e}{\bar{\Sigma}} + q_1 q_2 f \sinh\left(\frac{3q_2\Sigma_h}{2\bar{\Sigma}}\right)}{\left(\frac{\Sigma_e}{\bar{\Sigma}}\right)^2 + q_1 q_2 f \sinh\left(\frac{3q_2\Sigma_h}{2\bar{\Sigma}}\right)\frac{3\Sigma_h}{2\bar{\Sigma}}} \tag{24}$$

where $\Sigma_e = {}^{\sigma_e}/_{E} = {}^{(\sigma_{\theta\theta}-\sigma_{rr})}/_{E}$ is the dimensionless effective von Mises stress, $\bar{\Sigma} = {}^{\bar{\sigma}}/_{E}$ is the dimensionless matrix flow strength and $\Sigma_h = {}^{\sigma_h}/_{E}$ is the dimensionless hydrostatic stress.

Using the additive decomposition of the rate of deformation tensor, Eq. (1), together with equations (13)-(14) and (17)-(22), the following expressions are obtained:

$$v' = (v - \xi)\left[\Sigma'_{rr} - 2\nu\Sigma'_{\theta\theta} + (1-f)\left(\bar{\varepsilon}^p\right)'\tilde{N}_{rr}\right] \tag{25}$$

$$\frac{v}{\xi} = (v - \xi)\left[-\nu\Sigma'_{rr} + (1-\nu)\Sigma'_{\theta\theta} + (1-f)\left(\bar{\varepsilon}^p\right)'\tilde{N}_{\theta\theta}\right] \tag{26}$$

For a plastic loading, the relation between Σ_e and $\bar{\Sigma}$ is obtained when the flow potential, Φ, given in Eq. (5) is zero:

$$\left(\frac{\Sigma_e}{\bar{\Sigma}}\right)^2 + 2q_1 f \cosh\left(\frac{3q_2\Sigma_h}{2\bar{\Sigma}}\right) - 1 - (q_1 f)^2 = 0 \tag{27}$$

For a spherically symmetric problem, using Eq. (13), the dimensionless flow strength of the matrix material reads (see Eq. (6)):

$$\bar{\Sigma} = \bar{\Sigma}_{hom}\left(\bar{\varepsilon}^p, T\right) + \frac{l}{a}\left(\bar{\varepsilon}^p\right)' \tag{28}$$

where $\bar{\Sigma}_{hom} = {}^{\bar{\sigma}_{hom}}/_{E}$ is the dimensionless flow strength for homogeneous deformation given by (see Eq. (7)):

$$\bar{\Sigma}_{hom}\left(\bar{\varepsilon}^p, T\right) = \Sigma_0\left(1 + \frac{\bar{\varepsilon}^p}{\varepsilon_0}\right)^n\left(1 + b\exp^{-c\,(T_0-273)}\left(\exp^{-c(T-T_0)} - 1\right)\right) \tag{29}$$

with $\Sigma_0 = {}^{\sigma_0}/_{E}$ being the dimensionless initial yield stress of the matrix material. It is apparent from Eq. (28) that the effect of plastic strain gradients in the cavitation fields depends on the ratio between the length scale parameter l and the current cavity radius a (Danas et al., 2012), such that the size effect decreases as the cavity radius increases (the cavitation fields becoming independent of l for $a >> l$). In addition, recalling the geometric relation $h = a\tan\beta$, it is shown that increasing/decreasing the length scale parameter l has the same effect on the cavitation fields as decreasing/increasing the penetration depth h.

The evolution of porosity given by expression (9) is rewritten using Eqs. (14) and (21)-(22), as:

$$f' = (1-f)^2 \left(\tilde{N}_{rr} + 2\tilde{N}_{\theta\theta}\right) (\bar{\varepsilon}^p)' \tag{30}$$

Moreover, using the work equivalence principle, Eq. (8), and the time derivative introduced in Eq. (14), the energy balance given in Eq. (10) is rewritten as:

$$\frac{\rho C_p}{E} T' = \chi \, (1-f) \, \bar{\Sigma} \, (\bar{\varepsilon}^p)' \tag{31}$$

Furthermore, the mass conservation principle in Eulerian description, and in the absence of material spin, reads:

$$\dot{\rho} + \rho \, \left(d_{rr} + 2d_{\theta\theta}\right) = 0 \tag{32}$$

Using equations (1), (9), (14) and (19)-(20), we obtain:

$$\frac{\rho'}{\rho} = -\left[3(1-2\nu)\Sigma_h' + \frac{f'}{(1-f)}\right] \tag{33}$$

Integrating equation (33) from a given coordinate ξ to the elastic wave front ξ_w, where $f = f_0$, $\rho = \rho_0$, and $\Sigma_h = 0$ (see Fig. 1), a closed-form relation for the density ratio is obtained:

$$\frac{\rho}{\rho_0} = \frac{(1-f)}{(1-f_0)} \exp^{-3(1-2\nu)\Sigma_h} \tag{34}$$

In this model, Eqs. (16), (25)-(31) and (34) provide a system of three algebraic relations and six differential equations with nine unknowns $\left(v, \Sigma_{rr}, \Sigma_{\theta\theta}, \bar{\Sigma}, \bar{\Sigma}_{hom}, \bar{\varepsilon}^p, f, T, \rho\right)$.

The problem is completed with the following boundary conditions:

$$v = \frac{\tan\beta}{2} \quad \text{and} \quad \Sigma_{rr} = -P \quad \text{at} \quad \xi = 1 \quad \textit{(the cavity wall)} \tag{35}$$

and

$$v = 0 \quad \text{and} \quad \Sigma_{rr} = \Sigma_{\theta\theta} = 0 \quad \text{at} \quad \xi = \xi_w \quad \textit{(the elastic wave front)} \tag{36}$$

where $P = {}^{p}/_{E}$ is the dimensionless cavity pressure, see Fig. 1. Notice that the velocity boundary condition at

$\xi = 1$ corresponds to equation (12).

The integration is performed over the independent variable ξ, from ξ_w up to $\xi = 1$ (see Fig. 1). An iterative shooting method is used to enforce the velocity boundary condition at the cavity wall. The initial conditions, with an unknown constant, and the location of the elastic wave front, are determined employing the elastic solution derived by Durban and Masri (2004).

Note that considering the material strain rate sensitivity in the indentation model requires additional efforts, in line with the recent paper of dos Santos et al. (2020), who developed a time-dependent cavity expansion model for size-independent elasto-viscoplastic materials modeled with von Mises plasticity, and performed finite element simulations to estimate the extend of the transient behavior that precedes the quasi-constant velocity expansion of the cavity. For rate-dependent materials it is essential to identify the loading time from which $\dot{a}$ becomes quasi-constant because if the indentation process is much faster than the time required for the quasi-constant velocity cavity expansion to appear, then the constant velocity cavitation fields (hypothesis $\dot{a}$ = constant, see below Eq. (14)) do not describe the actual underlying physical phenomena. Thus, the extension of the dynamic cavity expansion model presented in this paper to rate-dependent materials is left for a future work, in which finite element simulations should also be performed.

4. Results

In this section we present the results obtained with the cavity expansion model developed in Section 3, for indentation velocities $\dot{h}$ ranging from 10^{-4} m/s to ≈ 400 m/s. We compare the theoretical predictions with the experimental results of Poole et al. (1996), McElhaney et al. (1998), Lim and Chaudhri (1999) and Hassani et al. (2020) to demonstrate the predictive capabilities of our analytical model. In addition, we perform parametric analyses to bring out the effects that inertia, size effect and initial porosity have on the material hardness and the elasto-plastic fields that develop near the indenter during the indentation process. We are aware that for the high indentation speeds investigated in this work it would have been pertinent to consider the material strain rate sensitivity, using a rate-dependent constitutive relation to describe the material flow strength. However, as mentioned before, material viscosity introduces a time scale into the cavity expansion process which prevents using a steady-state self-similar approach to solve the indentation problem (the cavitation fields become time dependent).

4.1. Fully dense materials

Figure 2 shows the evolution of the material hardness H with the indentation depth h predicted by the theoretical model, and the experimental data of Poole et al. (1996), McElhaney et al. (1998) and Lim and

Chaudhri (1999) for annealed OFHC copper (using pyramidal indenters) under quasi-static loading conditions. The experimental results show that the hardness decreases nonlinearly with the indentation depth, displaying a concave-upwards shape and almost reaching an horizontal asymptote for large values of h. The hardness at $h = 0.1$ μm is approximately five times greater than that at $h = 10$ μm. The dependence of H on the indentation depth shows the indentation size effect. In the theoretical model predictions, the hardness corresponds to the hydrostatic core pressure p (see Fig. 1 and equation (35)), the indentation velocity is $\dot{h} = 10^{-4}$ m/s (quasi-static loading) and the initial porosity f_0 is set to 0 (Poole et al. (1996); McElhaney et al. (1998); Lim and Chaudhri (1999) did not provide any measurement of the material porosity). The theoretical results are shown for different values of the length scale parameter $l = 0$, 10, 20, 30 and 50 nm. For $l = 0$, the cavity expansion model does not account for the size effect, and the hardness is independent of the indentation depth. For $l \neq 0$, the evolution of the hardness displays a concave-upwards shape (in qualitative agreement with the experiments), with increasing slope as the length scale parameter increases (the increase of l boosts the size effect in the indentation hardness). Notice that, while the hardness for small indentation depth of 0.1 μm is three times greater for $l = 50$ nm than for $l = 10$ nm, the value of H becomes practically independent of the length scale parameter for $h = 10$ μm. Although not shown here, similar trends are obtained for all other indentation speeds considered in this paper. Moreover, note that the theoretical predictions for $l = 20$ and 30 nm show reasonable quantitative agreement with the experiments, for the whole range of indentation depths investigated, providing some validity to the cavity expansion model and the simple gradient plasticity model used in this work.

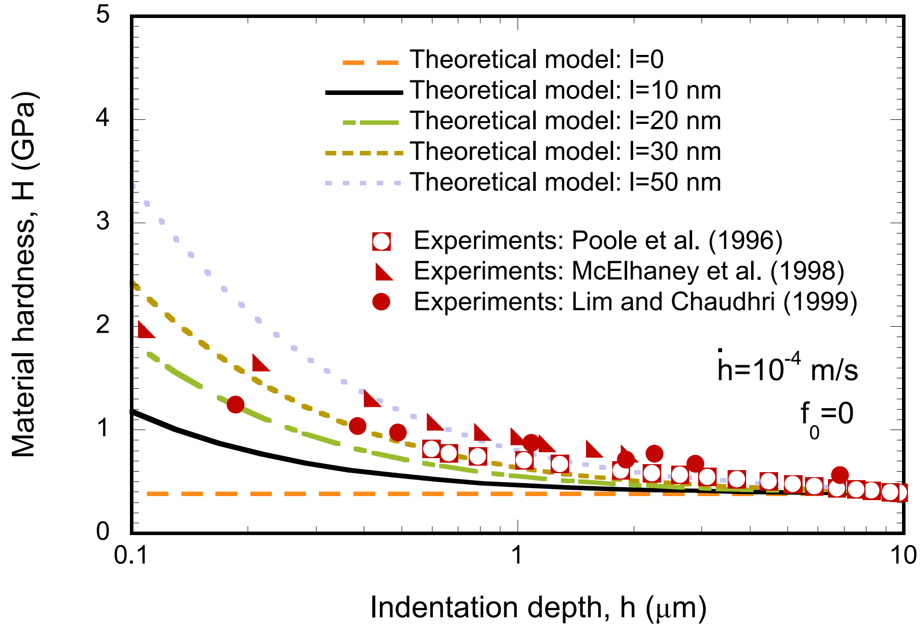

Figure 2: Evolution of the material hardness H with the indentation depth h predicted by the cavity expansion model for different values of the length scale parameter l = 0, 10, 20, 30 and 50 nm. The hardness corresponds to the hydrostatic core pressure p, the indentation velocity is $\dot{h} = 10^{-4}$ m/s and the initial porosity is $f_0 = 0$. The experimental data of Poole et al. (1996), McElhaney et al. (1998) and Lim and Chaudhri (1999) for annealed OFHC copper (using pyramidal indenter) under quasi-static loading conditions are also plotted.

The effect of the indentation speed on the theoretical predictions of the material hardness is investigated in Fig. 3(a). We now fix $l = 30$ nm as this value of the length scale parameter provided good agreement with the experiments in Fig. 2. Specifically, Fig. 3(a) shows the evolution of the hardness, H, with the indentation depth, h, for six different indentation speeds, $\dot{h} = 10^{-4}$, 50, 100, 200, 300 and 400 m/s. We consider the same range of indentation depths shown in Fig. 2 (note that 0.1 μm $\leq h \leq$ 10 μm is a typical range of indentation depth investigated in the literature, e.g. Shu and Fleck (1998)). The greater indentation speeds are similar to the velocities used in the dynamic experiments performed by Sundararajan and Tirupataiah (2006) and Hassani et al. (2020), among others. For all indentation speeds, the $H - h$ curves display a concave-upwards shape, with decreasing hardness as the indentation depth increases (as in Fig. 2). A key outcome is that the increase in the material hardness with the indentation speed is significant (only) for $\dot{h} \geq 100$ m/s, which suggests that this is the critical indentation speed above which inertial effects become important (at least for this cavity expansion model and the set of constitutive parameters considered). This conclusion is reinforced in Fig. 3(b), that displays the evolution of the material hardness, H, with the indentation speed, $\dot{h}$, at four values of the indentation depth, $h = 0.1$, 0.2, 1 and 3 μm. It is shown that the material hardness is virtually insensitive to the indentation speed for $\dot{h} \leq 100$ m/s. In addition, note that the increase in H that occurs for $\dot{h} \geq 100$ m/s is more pronounced as the indentation depth increases. This behavior is physically sound: the indentation depth increases the material volume displaced, and thus inertia effects, which are responsible for the increase in material hardness at high indentation speeds (in the absence of strain rate sensitivity, the jump in hardness at ≈ 100 m/s is attributed to inertia). Recall that assuming that the material is rate-independent has the advantage of isolating the effect of inertia in the cavitation fields at high strain rates.

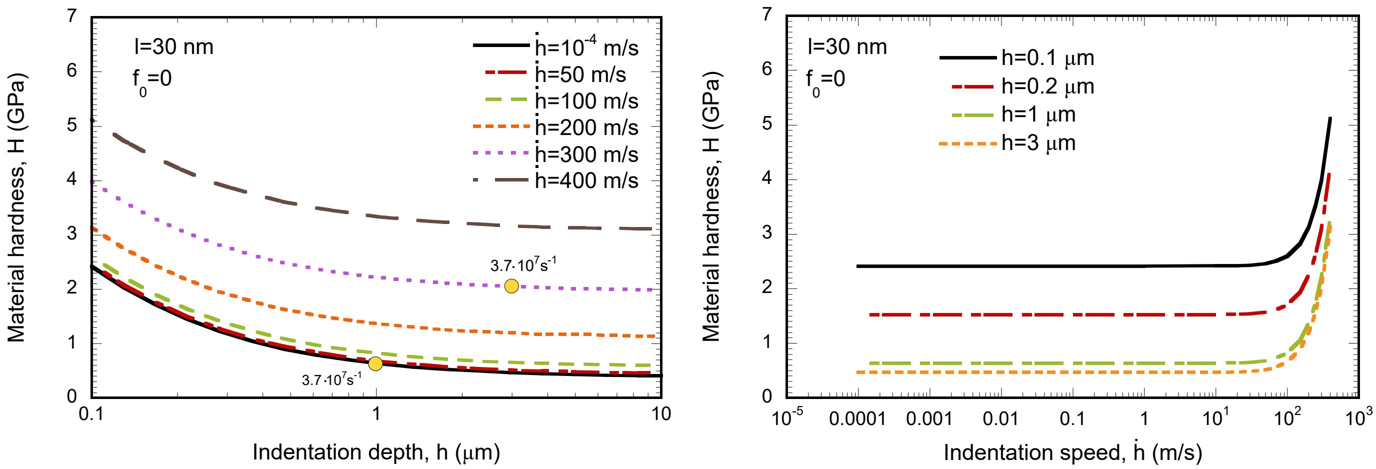

(a) (b)

Figure 3: Dynamic indentation model. The initial porosity, $f_0 = 0$ and the length scale parameter, $l = 30$ nm. (a) Evolution of the material hardness H with the indentation depth h for six indentation speeds. $\dot{h} = 10^{-4}$, 50, 100, 200, 300 and 400 m/s. (b) Evolution of the material hardness H with the indentation speed $\dot{h}$ at four values of the indentation depth, $h = 0.1$, 0.2, 1 and 3 μm.

Figure 4 displays the evolution of the material hardness, H, with the effective plastic strain rate, $\dot{\bar{\varepsilon}}^p$, predicted by the theoretical model, and the comparison with the experimental data in Hassani et al. (2020) for OFHC copper. Note that these authors did not provide any experimental measurement of the material porosity. Therefore, as in Fig. 3, the dynamic cavity expansion calculations are performed for $f_0 = 0$ while $l = 30$ nm. The theoretical results are shown at three values of the indentation depth, $h = 1$, 2 and 3 μm. The experimental results for strain rates lower than $10^4\,\mathrm{s}^{-1}$ were taken by Hassani et al. (2020) from uniaxial stress data reported in Armstrong and Walley (2008), and converted to hardness with a Tabor factor of 3. The experimental results for strain rates greater than $10^6\,\mathrm{s}^{-1}$ were obtained by Hassani et al. (2020) via high velocity impact indentations with spherical micro-particles of average diameter of $14\,\mu$m. The micro-particles were impacted onto copper targets at velocities near $v_i = 425 \pm 8$ m/s, leading to a maximum penetration depth of $2.79\,\mu$m. The characteristic strain rate of the impact indentation experiments was calculated by Hassani et al. (2020) according to the relation: $\dot{\bar{\varepsilon}}^p = v_i/\phi_p$, where ϕ_p is the diameter of the impacting particle. In contrast, the model predictions consider the effective plastic strain rate at the cavity wall, and a conical indenter (see Section 3). Nonetheless, there is a reasonable qualitative and quantitative agreement between the experimental data and the theoretical predictions, which provides additional validation for the analytical model developed in this paper. For the low strain rates, the theoretical predictions for $h = 1$ μm are closer to the experiments, however, at high strain rates, the best quantitative agreement with the tests is obtained for $h = 3$ μm. A key outcome is that the theoretical model captures the increase by a factor of 10 of the material hardness at high strain rates, making apparent the important role of inertia in high velocity indentation experiments, in agreement with the theoretical predictions previously shown in Fig. 3.

Note that the cavity expansion results for $h = 1$, 2 and 3 μm intersect at 10^7 s^{-1} such that for strain rates $< 10^7$ s^{-1}, the greater hardness is predicted for the smaller indentation depth, and vice versa for strain rates $> 10^7$ s^{-1}. As mentioned before, increasing the indentation depth increases the material volume displaced, and thus increases the inertial effects for a fixed value of the high strain rate. Notice that the relation between the strain rate and the indentation speed predicted by the theoretical model is linear, and the smaller the indentation depth, the higher the strain rate, see Fig. 5. Hence, in order to reach a fixed value of the high strain rate, the higher the indentation depth, the higher the indentation speed is required, which boosts the material hardness (the yellow markers in Figs. 3(a) and 5 correspond to a strain rate of $3.7 \cdot 10^7$ s^{-1}). On the other hand, Fig. 4 also shows that, while the increase in hardness predicted by the theoretical model at 10^7 s^{-1} seems to be too sharp, and a smoother evolution could have been expected (there is a sense of smooth increase of hardness in the experiments for $\approx 10^4$ s^{-1}), the absence of experimental data for strain rates ranging from 10^4 s^{-1} to 10^6 s^{-1} prevents drawing definite conclusions in this regard. Nevertheless, it is expected that including the strain rate sensitivity of the material in the cavity expansion model would provide a more gradual transition between the hardness obtained for 10^4 s^{-1} and 10^7 s^{-1}, and also greater values of H, leading to the theoretical predictions being closer to the experiments performed for $\dot{\bar{\varepsilon}}^p > 10^7$ s^{-1}. Note that the strain rate sensitivity would lead to an increase in the material flow strength with increasing strain rate, that shall trigger a gradual increase in the material hardness, particularly for strain rates below 10^7 s^{-1} (i.e. before inertia becomes the main contributor to material hardness). This point shall be addressed in future works, using an alternative method to the self-similar assumption used in this paper to solve the cavity expansion problem, see dos Santos et al. (2020).

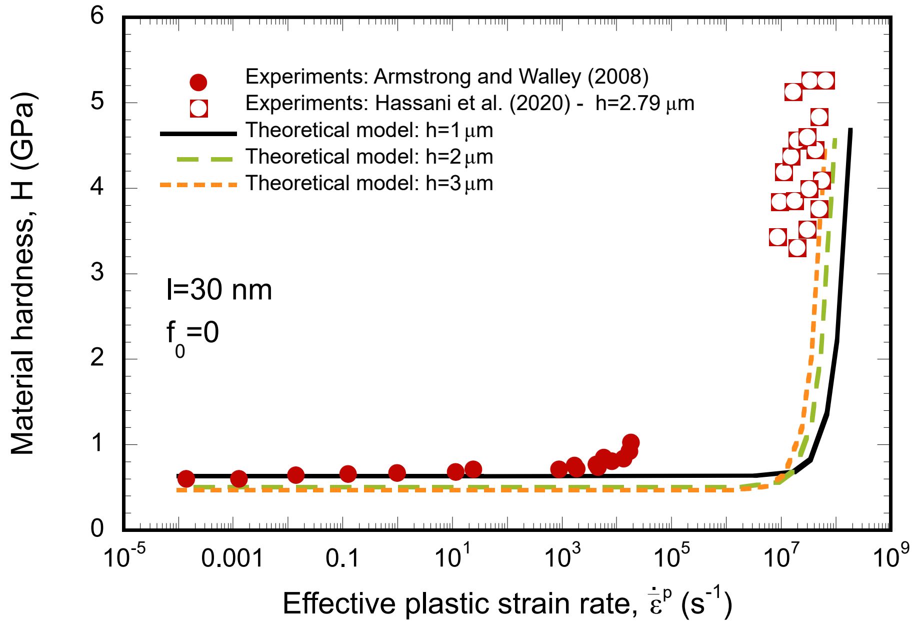

Figure 4: Evolution of the material hardness H with the effective plastic strain rate $\dot{\bar{\varepsilon}}^p$ predicted by the theoretical model and comparison with the experimental data reported in Hassani et al. (2020) for OFHC copper. In the theoretical model predictions, the initial porosity, $f_0 = 0$ and the length scale parameter, $l = 30$ nm. Theoretical results are shown at three values of the indentation depth, $h = 1$, 2 and 3 μm. The experimental results for strain rates lower than 10^4 s^{-1} were taken by Hassani et al. (2020) from uniaxial stress data of Armstrong and Walley (2008), and converted to hardness with a Tabor factor of 3. The experimental results for strain rates greater than 10^6 s^{-1} were obtained by Hassani et al. (2020) performing high velocity indentation experiments of spherical micro-particles impacting onto OFHC copper targets.

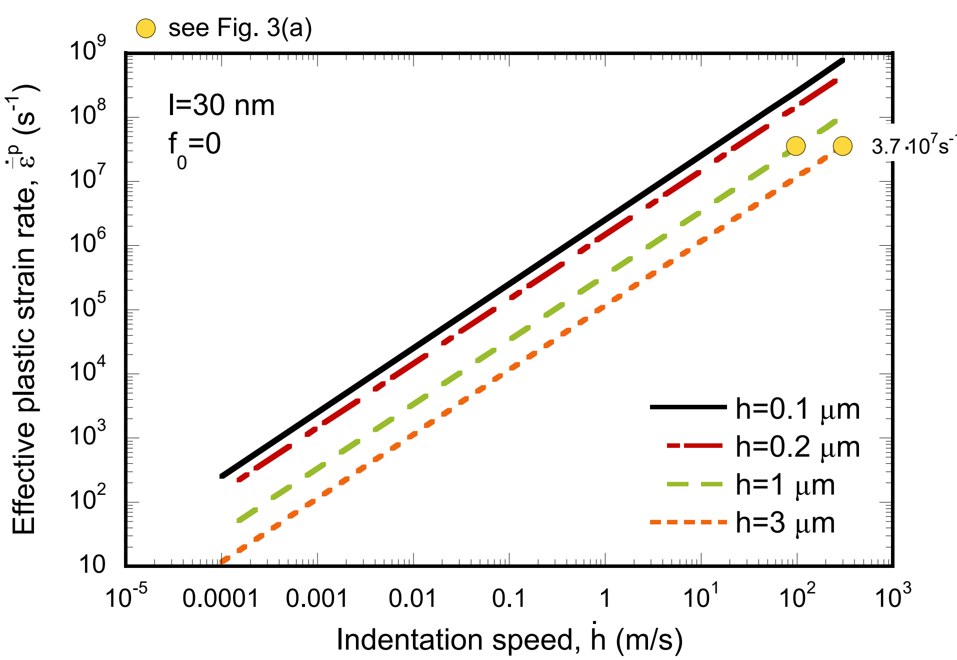

Figure 5: Dynamic indentation model. Effective plastic strain rate $\dot{\bar{\varepsilon}}^p$ versus indentation speed $\dot{h}$ at four values of the indentation depth, $h = 0.1$, 0.2, 1 and 3 μm. The initial porosity, $f_0 = 0$ and the length scale parameter, $l = 30$ nm.

The influence of the indentation speed on the cavitation fields that develop near the indenter is investigated in Fig. 6, which displays theoretical results for the evolution of the dimensionless effective stress Σ_e, the dimensionless radial stress Σ_{rr}, the effective plastic strain $\bar{\varepsilon}^p$, and the effective plastic strain rate $\dot{\bar{\varepsilon}}^p$ with the dimensionless radial coordinate ξ. The initial porosity, $f_0 = 0$, the indentation depth, $h = 0.1$ μm and the length scale parameter, $l = 30$ nm. Results are shown for five values of the indentation speed, $\dot{h} = 10^{-4}$, 50, 100, 200 and 300 m/s. The effective stress, the radial stress, the effective plastic strain and the effective plastic strain rate all decrease with the radial coordinate, displaying a concave-upwards shape, with the maximum values of Σ_e, Σ_{rr}, $\bar{\varepsilon}^p$ and $\dot{\bar{\varepsilon}}^p$ located at $\xi = 1$ (the cavity wall). Notice that the indentation speed hardly affects the effective stress Σ_e and the effective plastic strain $\bar{\varepsilon}^p$ (recall that the material is taken to be rate-independent). In contrast, the increase in $\dot{h}$ boosts the radial stress and the effective plastic strain rate near the cavity. Specifically, the radial stress at the cavity wall, which coincides with the material hardness (opposite sign), is 65% greater, in absolute value, for $\dot{h} = 300$ m/s than for $\dot{h} = 10^{-4}$ m/s. Moreover, the strain rate at $\xi = 1$ is six times greater for $\dot{h} = 300$ m/s than for $\dot{h} = 50$ m/s, which shows that at the cavity wall there is a linear relationship between the effective plastic strain rate and the indentation speed, as anticipated in Fig. 5. Notice that the effective plastic strain rate for $\dot{h} = 10^{-4}$ m/s is very low in comparison to the other indentation speeds (it is hardly noticeable in the graph), with a maximum value of ≈ 250 s^{-1}.

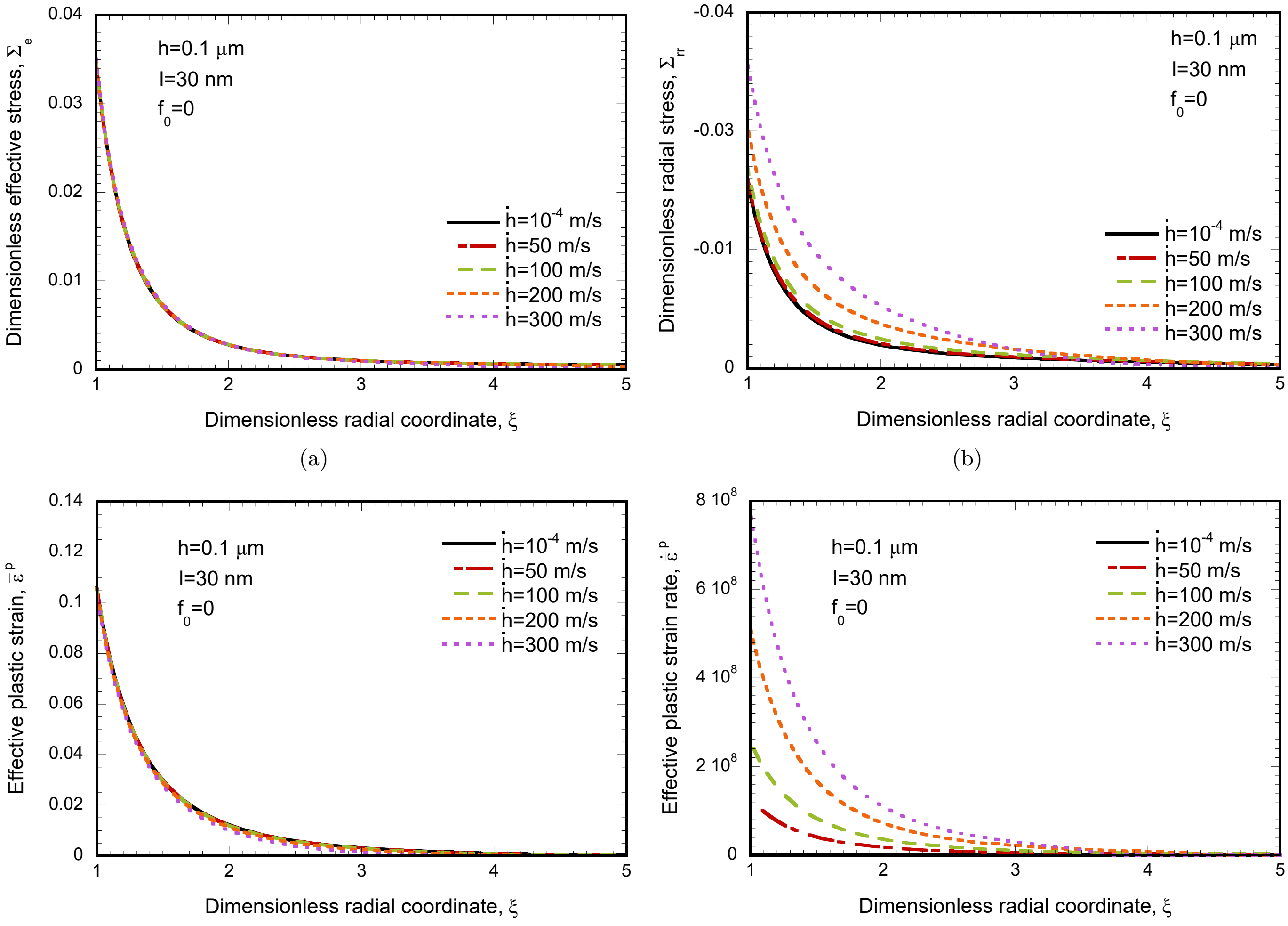

Figure 6: Dynamic indentation model. Results for (a) dimensionless effective stress Σ_e, (b) dimensionless radial stress Σ_{rr}, (c) effective plastic strain $\bar{\varepsilon}^p$ and (d) effective plastic strain rate $\dot{\bar{\varepsilon}}^p$ versus dimensionless radial coordinate ξ. The initial porosity, $f_0 = 0$, the length scale parameter, $l = 30$ nm and the indentation depth, $h = 0.1$ μm. Results are shown for five values of the indentation speed, $\dot{h} = 10^{-4}$, 50, 100, 200 and 300 m/s.

The influence of the indentation depth in the theoretical cavitation fields is investigated in Fig. 7, which shows the evolution of the dimensionless effective stress Σ_e, the dimensionless radial stress Σ_{rr}, the effective plastic strain $\bar{\varepsilon}^p$, and the effective plastic strain rate $\dot{\bar{\varepsilon}}^p$ with the dimensionless radial coordinate ξ, at four values of h: 0.1 (the value taken in Fig. 6), 0.2, 1 and 3 μm. The results correspond to $\dot{h} = 300$ m/s (the greatest value shown in Fig. 6), while $f_0 = 0$ and $l = 30$ nm. Figure 7(a) shows that the $\Sigma_e - \xi$ curves shift downwards as the indentation depth increases, such that at the cavity wall the effective stress at $h = 0.1$ μm is ≈ 11 times greater than that at $h = 3$ μm. In contrast, the accumulated effective plastic strain is greater as the indentation depth increases (reaching ≈ 0.13 in the case of $h = 3$ μm), with slightly greater gradients of $\bar{\varepsilon}^p$ as h increases, see Fig. 7(c). Similar trends for the dependence of the effective stress and the effective plastic strain with the indentation depth were obtained from the quasi-static finite element calculations performed by

Danas et al. (2012) for fully-dense materials (see the discussion of Fig. 10 therein). Moreover, Fig. 7(b) shows that the radial stress decreases, in absolute value, as the indentation depth increases. At the cavity wall, where the radial stress equals the material hardness, the absolute value of Σ_{rr} at $h = 0.1$ μm is twice greater than that at $h = 3$ μm. This is consistent with the results presented in Fig. 3(a). Note that, in absence of any size effect, effective stress, radial stress and effective plastic strain are independent of the indentation depth, so that these results bring out the important role of the size effect on the cavitation fields that develop during dynamic indentation. The relaxation of the material as the indentation proceeds is illustrated in Fig. 7(d), which shows that the effective plastic strain rate decreases with the increasing indentation depth. At the cavity wall, $\xi = 1$, the value of $\dot{\bar{\varepsilon}}^p$ at $h = 0.1$ μm is approximately 20 times greater than that at $h = 3$ μm. Note that the effective plastic strain rate depends on the indentation depth regardless of whether the size effect is considered or not.

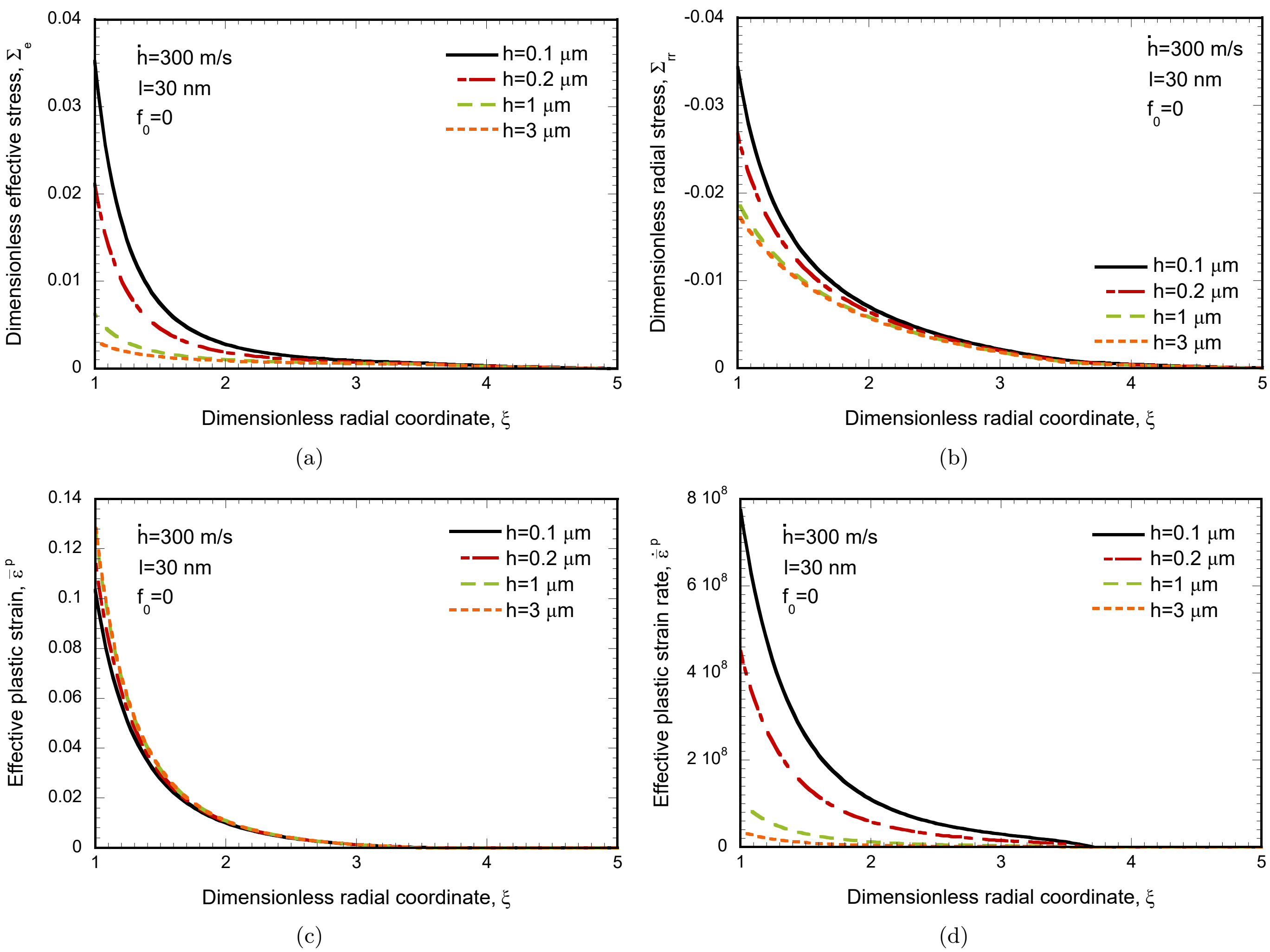

Figure 7: Dynamic indentation model. Results for (a) dimensionless effective stress Σ_e, (b) dimensionless radial stress Σ_{rr}, (c) effective plastic strain $\bar{\varepsilon}^p$ and (d) effective plastic strain rate $\dot{\bar{\varepsilon}}^p$ versus dimensionless radial coordinate ξ. The initial porosity, $f_0 = 0$, the length scale parameter, $l = 30$ nm and the indentation speed, $\dot{h} = 300$ m/s. Results are shown at four values of the indentation depth, $h = 0.1$, 0.2, 1 and 3 μm.

4.2. Porous materials

Figure 8 shows the predictions of the cavity expansion model for the evolution of the material hardness, H, with the indentation depth, h, for a fixed length scale parameter, $l = 30$ nm, and three values of the initial porosity, $f_0 = 0$ (fully dense material), 0.05 and 0.1. Similar range of initial void volume fractions has been considered by Fleck et al. (1992) to study quasi-static indentation of porous solids. Moreover, other authors, e.g. Czarnota et al. (2017), have also investigated initial void volume fractions as high as 0.1 to bring out the role of porosity on the dynamic response of porous metallic materials subjected to impact loading conditions. Note that exploring such a wide spectrum of initial void volume fractions allows us to elucidate the role of porosity on the cavitation fields and material hardness, and to obtain trends for the interplay between size effects and initial void volume fraction. In addition, sintered and additively manufactured metals may contain initial porosity ranging from 1% to 10% (e.g. see Aboulkhair et al. (2014)), so that the range of void volume fractions investigated in this work is representative of some engineering materials, if not all. As shown in Fig. 8(a), for the indentation speed, $\dot{h} = 10^{-4}$ m/s, irrespective of the initial porosity, the $H - h$ curves show a concave-upwards shape (as in Figs. 2 and 3(a)). For $\dot{h} = 10^{-4}$ m/s, the hardness of the material only increases slightly with decreasing initial porosity. In contrast, the results in Fig. 8(b) show that for $\dot{h} = 300$ m/s the influence of the initial porosity on the material hardness is significant and dependent on the indentation depth, such that the differences between the $H - h$ curves obtained for different values of f_0 increase as h increases. In fact, the slope of the $H - h$ curves increases with the porosity, bringing out that f_0 slightly broadens the range of the indentation depths for which size effect plays a role on the dynamic material hardness.

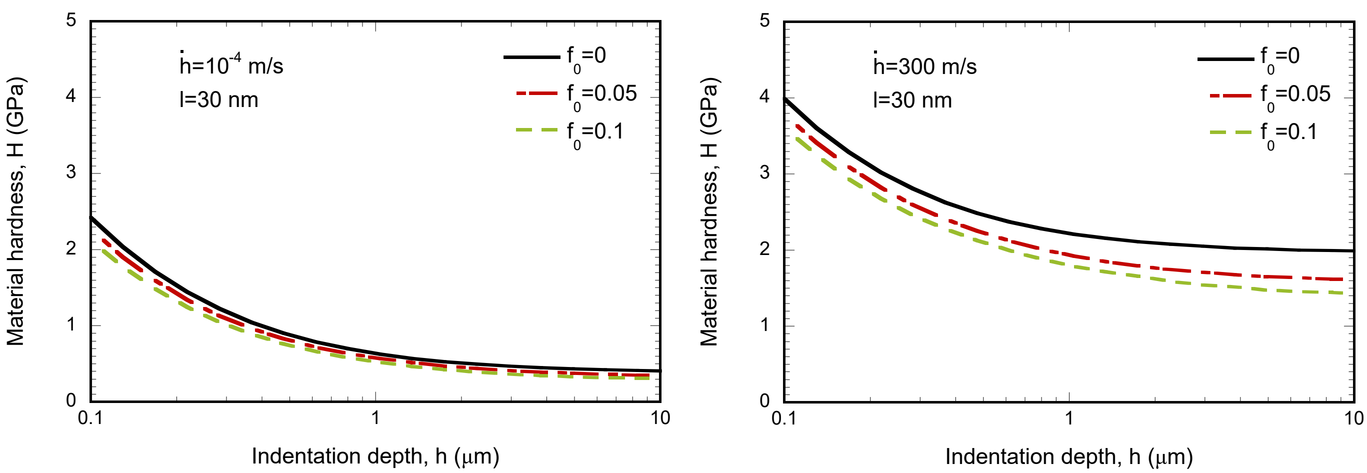

(a) (b)

Figure 8: Dynamic indentation model. Evolution of the material hardness H with the indentation depth h for three values of the initial porosity, $f_0 = 0$ (fully dense material), 0.05 and 0.1. The length scale parameter is $l = 30$ nm, and the indentation speed is: (a) $\dot{h} = 10^{-4}$ m/s and (b) $\dot{h} = 300$ m/s.

Figure 9 illustrates the evolution of the material hardness, H, with the length scale parameter, l, for three values of the initial porosity, $f_0 = 0$, 0.05 and 0.1. The indentation speed, $\dot{h} = 300$ m/s. The material hardness increases non-linearly with the parameter l, displaying a concave-upwards shape. The comparison of the results at $h = 0.1$ and 1 μm presented in Figs. 9(a) and 9(b), respectively, shows that the increase in hardness with the length scale parameter, i.e. with the size effect, is more important for the lower indentation depth, in agreement with the results shown in Fig. 2. In addition, the comparison of Figs. 8 and 9 shows that increasing the length scale l has the same effect on the material hardness as decreasing the indentation depth, h (as anticipated in Section 3, see the discussion below equation (29)). Moreover, notice that the decrease in the hardness with an increase in the initial porosity is more important for small values of the parameter l, which illustrates that size effect reduces the effect of the porosity on the cavitation fields (this conclusion will be further discussed in Figs. 10 and 11).

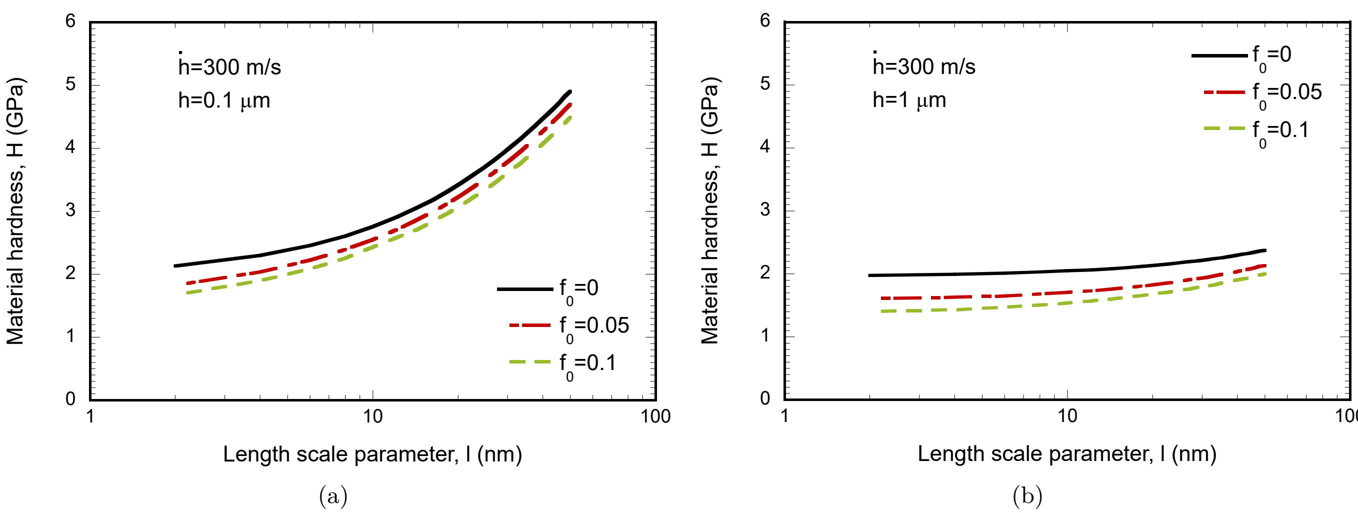

Figure 9: Dynamic indentation model. Evolution of the material hardness H with the length scale parameter l for three values of the initial porosity, $f_0 = 0$ (fully dense material), 0.05 and 0.1. The indentation speed is $\dot{h} = 300$ m/s, and the indentation depth is: (a) $h = 0.1$ μm and (b) $h = 1$ μm.

The role of the initial porosity on the cavitation fields is illustrated in Fig. 10, which shows the evolution of the dimensionless effective stress Σ_e, the dimensionless radial stress Σ_{rr}, the effective plastic strain $\bar{\varepsilon}^p$, and the effective plastic strain rate $\dot{\bar{\varepsilon}}^p$ with the dimensionless radial coordinate ξ, for three values of f_0: 0 (fully dense material), 0.05 and 0.1. The indentation speed, $\dot{h} = 300$ m/s, the indentation depth, $h = 0.1$ μm and the length scale parameter, $l = 30$ nm. The influence of the initial material porosity on the cavitation fields is generally small, and the evolution of Σ_e, Σ_{rr}, $\bar{\varepsilon}^p$ and $\dot{\bar{\varepsilon}}^p$ with ξ shows the same concave-upwards shape for the three values of f_0 considered. Specifically, the effective stress and the effective plastic strain are hardly affected by the initial porosity, and the curves obtained for different values of f_0 virtually overlap with each other, see Figs. 10(a) and 10(c). Moreover, the radial stress, Fig. 10(b), slightly decreases with the initial porosity, especially for intermediate values of ξ. On the other hand, Fig. 10(d) shows that the $\dot{\bar{\varepsilon}}^p - \xi$ curves intersect for an intermediate value of ξ, such that the greatest effective plastic strain rate corresponds to $f_0 = 0.1$ near the cavity wall, and to $f_0 = 0$ for $\xi > 2.2$.

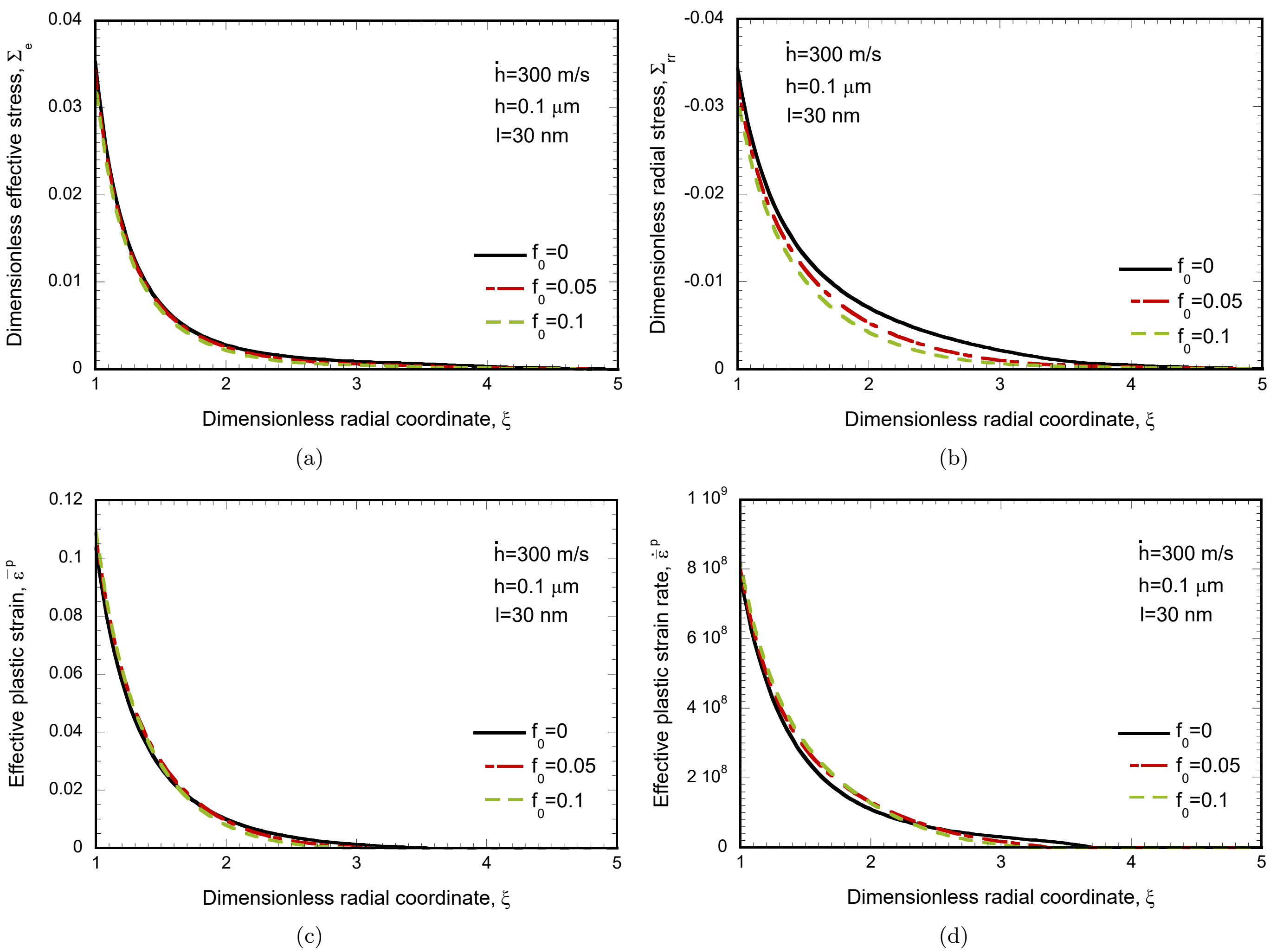

Figure 10: Dynamic indentation model. Results for (a) dimensionless effective stress Σ_e, (b) dimensionless radial stress Σ_{rr}, (c) effective plastic strain $\bar{\varepsilon}^p$ and (d) effective plastic strain rate $\dot{\bar{\varepsilon}}^p$ versus dimensionless radial coordinate ξ, for three values of f_0: 0 (fully dense material), 0.05 and 0.1. The indentation speed, $\dot{h} = 300$ m/s, the indentation depth, $h = 0.1$ μm and the length scale parameter, $l = 30$ nm.

In comparison with Fig. 10, the results presented in Fig. 11 correspond to a greater indentation depth $h = 1$ μm. The initial porosity, unlike in the case of $h = 0.1$ μm, significantly affects the distributions of effective stress Σ_e, radial stress Σ_{rr}, effective plastic strain $\bar{\varepsilon}^p$ and effective plastic strain rate $\dot{\bar{\varepsilon}}^p$. Specifically, the effective stress at the cavity wall is greater for $f_0 = 0.1$, and it decreases faster as the initial porosity increases, see Fig. 11(a). In contrast, the greater value of Σ_{rr} obtained at the cavity wall for the fully dense material is accompanied by a more sustained drop in the radial stress as the porosity decreases. Moreover, Fig. 11(c) shows that, while the effective plastic strain at the cavity wall increases with the porosity, the plastic zone is smaller as f_0 increases, revealing that porosity favors localization of plastic deformation. Similarly, Fig. 11(d) shows that the effective plastic strain rate is greater at the cavity wall, and decreases faster with the radial coordinate, as the initial porosity increases. Notice also that, unlike the results for the fully dense material, the $\dot{\bar{\varepsilon}}^p - \xi$ curves for $f_0 = 0.05$ and 0.1 turn from concave-downwards to concave-upwards for an intermediate value of the radial coordinate, revealing the important effect of porosity in the strain rate fields that develop near the indenter. The key outcome from Figs. 10 and 11 is that increasing the indentation depth, i.e. decreasing the size effect, boosts the influence of the porosity on the cavitation fields. Although not shown here, the same overall trends are obtained for low indentation speed, $\dot{h} = 10^{-4}$ m/s, as well.

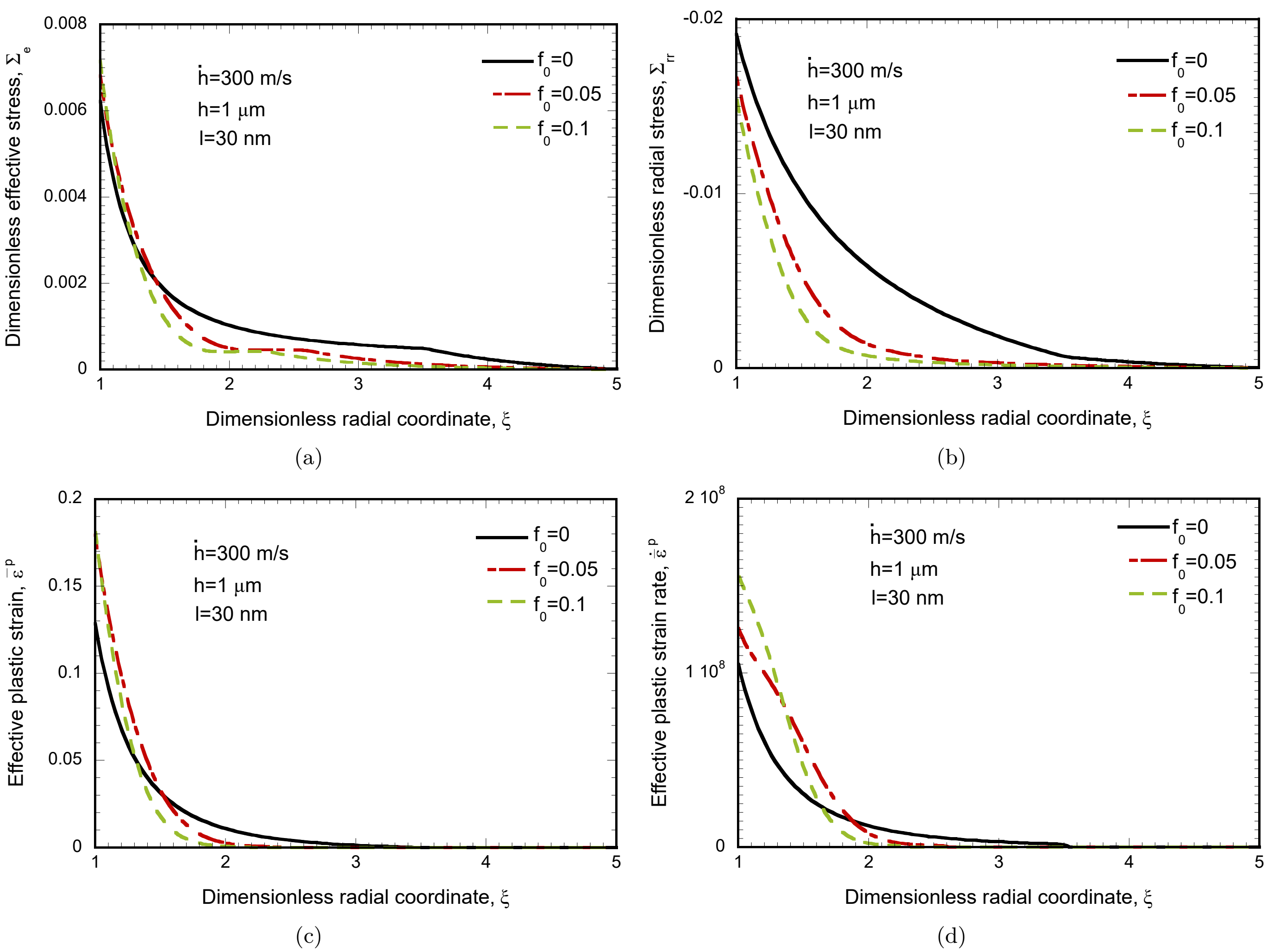

Figure 11: Dynamic indentation model. Results for (a) dimensionless effective stress Σ_e, (b) dimensionless radial stress Σ_{rr}, (c) effective plastic strain $\bar{\varepsilon}^p$ and (d) effective plastic strain rate $\dot{\bar{\varepsilon}}^p$ versus dimensionless radial coordinate ξ, for three values of f_0: 0 (fully dense material), 0.05 and 0.1. The indentation speed, $\dot{h} = 300$ m/s, the indentation depth, $h = 1$ μm and the length scale parameter, $l = 30$ nm.

5. Conclusions

In this work we have developed a dynamic self-similar cavity expansion model to analyze the high rate indentation response of elasto-plastic porous materials while accounting for the plastic strain gradient induced size effect. The main novelty of the model developed herein is the incorporation of the plastic strain gradient induced size effect in the dynamic cavity expansion model for elasto-plastic porous materials. The predictions of the cavity expansion model for the material hardness, for indentation depths varying from 0.1 μm to 10 μm, and speeds yielding a variation in the strain rates from 10^{-4} s^{-1} to 10^{8} s^{-1}, are compared against the available experimental results on OFHC copper. We note that despite several simplifying assumptions, the predictions of our cavity expansion model show a reasonable agreement with the experimentally measured material hardness over such a wide range of indentation depths and strain rates. We have also carried out parametric analyses to elucidate the specific roles of inertia, size effect and initial porosity on the material hardness and the cavitation fields that develop during the indentation process. The key conclusions of this work are as follows:

- There exists a critical indentation speed ($\approx$ 100 m/s for the set of constitutive parameters considered) above which the inertial effect becomes extremely important and the material hardness increases rapidly.
- The rapid increase in the material hardness at very high strain rates becomes more pronounced as the indentation depth increases, highlighting the fact that the inertial effect increases with increasing indentation depth.
- Incorporation of the plastic strain gradient induced size effect in the dynamic cavity expansion model leads to a decrease in the radial stress near the cavity wall with increasing indentation depth, while in the absence of any size effect the radial stress will be independent of the indentation depth.
- The effect of initial porosity on the hardness of the material (i.e the hardness decreases with increasing initial porosity) increases with increasing indentation speed, and at sufficiently high indentation speeds the effect of initial porosity on the hardness of the material increases with increasing indentation depth.
- The effect of initial porosity on the hardness of the material decreases with increasing value of the length scale parameter, i.e. increasing size effect.

Acknowledgements

TdS wishes to acknowledge the support of FAPERGS, Fundação de Amparo ã Pesquisa do Estado do Rio Grande do Sul, grant agreement $19/2551 - 0001054 - 0$.

JAR-M acknowledges the financial support obtained from the European Research Council (ERC) under the European Union's Horizon 2020 research and innovation programme. Project PURPOSE, grant agreement 758056.

References

Aboulkhair, N.T., Everitt, N.M., Ashcroft, I., Tuck, C., 2014. Reducing porosity in AlSi10Mg parts processed by selective laser melting. Additive Manufacturing 1-4, 77 – 86. Inaugural Issue.

Aifantis, E.C., 1984. On the Microstructural Origin of Certain Inelastic Models. Journal of Engineering Materials and Technology 106, 326–330.

Armstrong, R.W., Walley, S.M., 2008. High strain rate properties of metals and alloys. International Materials Reviews 53, 105–128.

Arreguin-Zavala, J., Milligan, J., Davies, M.I., Goodes, S.R., Brochu, M., 2013. Characterization of nanostructured and ultrafine-grain aluminum-silicon claddings using the nanoimpact indentation technique. JOM 65, 763–768.

Chen, J., Yuan, H., 2002. A micro-mechanical damage model based on gradient plasticity: algorithms and applications. International Journal for Numerical Methods in Engineering 54, 399–420.

Cohen, T., Durban, D., 2013a. Fundamental solutions of cavitation in porous solids: a comparative study. Acta Mechanica 224, 1695–1707.

Cohen, T., Durban, D., 2013b. Hypervelocity cavity expansion in porous elastoplastic solids. Journal of Applied Mechanics 80, 011017.

Czarnota, C., Molinari, A., Mercier, S., 2017. The structure of steady shock waves in porous metals. Journal of the Mechanics and Physics of Solids 107, 204 – 228.

Danas, K., Deshpande, V., Fleck, N., 2012. Size effects in the conical indentation of an elasto-plastic solid. Journal of the Mechanics and Physics of Solids 60, 1605 – 1625.

Durban, D., Masri, R., 2004. Dynamic spherical cavity expansion in a pressure sensitive elastoplastic medium. International Journal of Solids and Structures 41, 5697–5716.

Fleck, N., Otoyo, H., Needleman, A., 1992. Indentation of porous solids. International Journal of Solids and Structures 29, 1613 – 1636.

Gao, X.L., 2006. An expanding cavity model incorporating strain-hardening and indentation size effects. International Journal of Solids and Structures 43, 6615 – 6629.

Gao, X.L., Jing, X., Subhash, G., 2006. Two new expanding cavity models for indentation deformations of elastic strain-hardening materials. International Journal of Solids and Structures 43, 2193 – 2208.

Hassani, M., Veysset, D., Nelson, K.A., Schuh, C.A., 2020. Material hardness at strain rates beyond 106 s-1 via high velocity microparticle impact indentation. Scripta Materialia 177, 198 – 202.

Johnson, K.L., 1970. The correlation of indentation experiments. Journal of the Mechanics and Physics of Solids 18, 115–126.

Lim, Y.Y., Chaudhri, M.M., 1999. The effect of the indenter load on the nanohardness of ductile metals: An experimental study on polycrystalline work-hardened and annealed oxygen-free copper. Philosophical Magazine A 79, 2979–3000.

Lu, J., Suresh, S., Ravichandran, G., 2003. Dynamic indentation for determining the strain rate sensitivity of metals. Journal of the Mechanics and Physics of Solids 51, 1923 – 1938. Proceedings of a Symposium on Dynamic Failure and Thin Film Mechanics, honoring Professor L.B. Freund.

Mata, M., Casals, O., Alcalá, J., 2006. The plastic zone size in indentation experiments: The analogy with the expansion of a spherical cavity. International Journal of Solids and Structures 43, 5994 – 6013.

McElhaney, K.W., Vlassak, J.J., Nix, W.D., 1998. Determination of indenter tip geometry and indentation contact area for depth-sensing indentation experiments. Journal of Materials Research 13, 1300–1306.

Mok, C.H., Duffy, J., 1964. The behavior of metals at elevated temperatures under impact with a bouncing ball. International Journal of Mechanical Sciences 6, 161 – 175.

Mok, C.H., Duffy, J., 1965. The dynamic stress-strain relation of metals as determined from impact tests with a hard ball. International Journal of Mechanical Sciences 7, 355 – 371.

Poole, W., Ashby, M., Fleck, N., 1996. Micro-hardness of annealed and work-hardened copper polycrystals. Scripta Materialia 34, 559 – 564.

Qin, L., Li, H., Shi, X., Beake, B.D., Xiao, L., Smith, J.F., Sun, Z., Chen, J., 2019. Investigation on dynamic hardness and high strain rate indentation size effects in aluminium (110) using nano-impact. Mechanics of Materials 133, 55 – 62.

dos Santos, T., Brezolin, A., Rossi, R., Rodríguez-Martínez, J.A., 2020. Modeling dynamic spherical cavity expansion in elasto-viscoplastic media. Acta Mechanica 231, 2381–2397.

Shu, J.Y., Fleck, N.A., 1998. The prediction of a size effect in microindentation. International Journal of Solids and Structures 35, 1363 – 1383.

Subhash, G., Koeppel, B.J., Chandra, A., 1999. Dynamic indentation hardness and rate sensitivity in metals. Journal of Engineering Materials and Technology 121, 257–263.

Sundararajan, G., Tirupataiah, Y., 2006. The localization of plastic flow under dynamic indentation conditions: I. experimental results. Acta Materialia 54, 565 – 575.

Tanner, A.B., McDowell, D.L., 1999. Deformation, temperature and strain rate sequence experiments on ofhc cu. International Journal of Plasticity 15, 375 – 399.

Tirupataiah, Y., Sundararajan, G., 1991. A dynamic indentation technique for the characterization of the high strain rate plastic flow behaviour of ductile metals and alloys. Journal of the Mechanics and Physics of Solids 39, 243 – 271.

Trelewicz, J.R., Schuh, C.A., 2008. The hall-petch breakdown at high strain rates: Optimizing nanocrystalline grain size for impact applications. Applied Physics Letters 93, 171916.